252
A6

Reprinted from

PLASMA PHYSICS–ACCELERATORS–THERMONUCLEAR RESEARCH

Journal of Nuclear Energy Part C

PERGAMON PRESS

OXFORD • LONDON • NEW YORK • PARIS

Plasma Physics (Journal of Nuclear Energy Part C) 1965, Vol. 7, pp. 47 to 67. Pergamon Press Ltd. Printed in N. Ireland

NUMERICAL COMPUTATIONS FOR ION PROBE CHARACTERISTICS IN A COLLISIONLESS PLASMA

F. F. CHEN
Princeton University, Princeton, N.J.

(*Received* 22 *June* 1964)

Abstract—Numerical results in ranges of experimental interest are presented in graphical form for the potential profile around negatively biased spherical and cylindrical probes in a collisionless plasma and for the saturation ion current-voltage characteristics. The computations were made on the basis of the theories of ALLEN, BOYD and REYNOLDS (1957) for zero ion temperature and of BERNSTEIN and RABINOWITZ (1959) for monoenergetic ions. These theories are useful primarily for small probes. For large probes the theory of LAM (1964) is applicable. For completeness we have also included whatever curves are necessary for the use of LAM's theory.

1. INTRODUCTION

THE recent boundary-layer analysis of LAM (1964) puts the theory of electrostatic probes in a collisionless plasma into definitive form. As long as collisions and magnetic fields do not play a role, and as long as the experimental difficulties of particle trapping and of reflection, secondary emission, changes of work function, and so forth at the probe surface can be overcome, the current to a biased probe can now be predicted rigorously by theory. However, in some situations tedious numerical computation is necessary. It is the purpose of this paper to assemble under a single cover such numerical results as may be needed by an experimentalist, in a form which is convenient to use.

The situation may be summarized as follows. For collection of the hotter species, usually electrons, the original theory of LANGMUIR (1961) is valid. For collection of the colder species, usually ions, LANGMUIR's orbital theory may still be used if $a \ll h$ (symbols are defined in Section 2). The case $a \gg h$ is covered by the theory of LAM (1964). In the limit of large a or small η_p this theory reduces to the well-known result of BOHM, BURHOP and MASSEY (1949) and of WENZL (1950). LAM's theory is more rigorous and more convenient to use than the earlier theory by WENZL. The case $a \approx h$ is covered by the theory of ALLEN, BOYD and REYNOLDS (1957) for $\beta = 0$ and by the theory of BERNSTEIN and RABINOWITZ (1959) for $0 < \beta < 1$. This case is the troublesome one and necessitates the numerical computations whose results are presented in this paper.

We have concentrated attention on the simpler equations of ALLEN *et al.* which give a fairly good approximation for $\beta < 0{\cdot}1$, especially in the spherical case. In addition to the probe characteristics we have given the potential distributions so that the reader may make his own cross-plots if that is necessary. The computations were made on an IBM 7090 and cover a wider range of parameters than given by ALLEN *et al.* In the case of the BERNSTEIN and RABINOWITZ theory, we have extended the original computations only in the cylindrical case. However, we wish to point out that because of a number of misprints the original paper of BERNSTEIN and RABINOWITZ gives incorrect numerical results and should be used only for the formulation of the theory.

The curves contained herein replace the need to approximate by patching the BOHM current to the $V^{3/2}$ space-charge law. This procedure, used previously by KAGAN and PEREL (1953), SCHULZ and BROWN (1955), BOYD and THOMPSON (1959) and ICHIMIYA, TAKAYAMA and AONO (1960), is both more laborious and less accurate.

The proper theory to use for saturation ion currents is shown in Table 1 for

TABLE 1

Ion distribution	β	Geom.	$a \ll h$	$a \approx h$			$a \gg h$		
			all η_p	$\eta_p \gg 1$	$1 < \eta_p < 5$	$\eta_p < 1$	$\eta_p \gg 1$	$1 < \eta_p < 5$	$\eta_p < 1$
—	0	Sph.		ABR*			LAM* (ABR)		LAM
		Cyl.		C*			C*		
Mono-energetic	$\ll 1$	Sph.	L-O	BR*			LAM* (B, W)	LAM†	LAM
		Cyl.	L-O	BR*		L-O	LAM* (W)	LAM†	LAM
	≈ 1	Sph.	L-O	BR			LAM* (B, W)	LAM†	LAM
		Cyl.	L-O	BR		L-O	LAM* (W)	LAM†	LAM
	$\gg 1$	Sph.	L-O	BR		L-O	L-S		L-O
		Cyl.	L-O	BR		L-O	L-S		L-O
Maxw.	$\ll 1$	Sph.	L-O	BR†			BR†		
		Cyl.	L-O	BR†		L-O	BR†		
	≈ 1	Sph.	L-O	H (BR†)			H (BR†)		
		Cyl.	L-O	H (BR†)			H (BR†)		
	$\gg 1$	Sph.	L-O	BR†		L-O	L-S		L-O
		Cyl.	L-O	BR†		L-O	L-S		L-O

* Numerical computations available in this paper.
† Formalism indicated only.
( ) Superseded work; L-O, LANGMUIR (1961) orbital-motion theory; L-S, LANGMUIR (1961) sheath theory; ABR, ALLEN, BOYD and REYNOLDS (1957); BR, BERNSTEIN and RABINOWITZ (1959); LAM, LAM (1964); B, BOHM, BURHOP and MASSEY (1949); W, WENZL (1950); H, HALL (1964); C, CHEN (present paper).

various ranges of parameters. The probe voltage η_p enters because it affects the distribution of the electrons. For $\eta_p \gg 1$, the electron distribution may be considered Maxwellian. For η_p less than about 1/2 or 1, the quasi-neutral solution holds everywhere, and probe theory is particularly simple. For $1 < \eta_p < 5$, the deviation from a Maxwellian distribution due to the loss of electrons to the probe must be taken into account. Although this poses no problem in principle, it complicates the computations. It is understood that the above remarks apply equally well to electron collection when the ions are nearly Maxwellian; however, for saturation electron currents the need for Table 1 does not arise unless $T_e < T_i$. The case $1 < \eta < 5$ is, of course, interesting for the computation of the floating potential.

Although our computations have been made only for monoenergetic ions, it is clear that the results for a Maxwellian distribution will not be appreciably different for $\beta \ll 1$, since the dependence on ion energy is slight. On the other hand, for $\beta \gg 1$ the probe current depends primarily on kT_i and is given by LANGMUIR's sheath theory for a Maxwellian distribution. The transition case $\beta \approx 1$ is not well covered by any simple theory. The simple sheath theory fails because the accelerating electric field outside the sheath is neglected; the BERNSTEIN and RABINOWITZ (1959) theory fails because a monoenergetic distribution is no longer a good approximation. This gap in the theory has been plugged recently by HALL (1964), who has found a method to integrate numerically the BERNSTEIN and RABINOWITZ equations for a Maxwellian distribution.

Finally, we wish to point out that whenever possible spherical probes should be used in preference to cylindrical probes for the following reasons:

(i) The disturbance of the plasma by the probe is smaller for a sphere because the potential falls off faster with radius.

(ii) For a given radius, a cylindrical probe is more likely to trap ions in closed orbits; that is, it must be operated at lower potential than a spherical probe. Conversely, for a given η_p a cylindrical probe must be made larger in diameter in order to avoid ion trapping.

(iii) Spherical probes are not sensitive to the distribution of angular momenta assumed at infinity.

(iv) For spherical probes the theory is simpler, and numerical computations are easier to carry out.

These remarks are of course not applicable in the presence of a strong magnetic field.

2. DEFINITIONS

C.G.S.–e.s.u. are used. The current I_i is the particle current *multiplied by the charge number* Z *of the particle*. The subscript p indicates probe surface; the subscript 0 indicates absorption radius; and the subscript 1 indicates the radius where the quasi-neutral solution breaks down.

$\eta = -\mathrm{e}V/kT_e$ (normalized potential)
$\xi = r/h$ (normalized radius)
$\xi_p = r_p/h$ or a/h (normalized probe radius)
$h = (kT_e/4\pi n_0 e^2)^{1/2}$ (Debye length)
$n_0 =$ plasma density at ∞
$E_i =$ ion energy at ∞, for a monoenergetic distribution
$\beta = E_i/ZkT_e$ (normalized ion energy)
$Z =$ charge number of the ions
$J = I_i(e^2/kT_e)(m_i/2ZkT_e)^{1/2}$ (normalized ion current for *spheres*)
$J = I_i(e/kT_e)(m_i/2\pi n_0 Z)^{1/2}$ (normalized ion current for *cylinders*)
$I_i =$ total ion current to probe for *spheres*
$I_i =$ ion current per unit length to probe for *cylinders*
$J\xi_p = I_i r_p(\mathrm{e}/kT_e)^2(2m_i kT_e/Z)^{1/2}$ (another useful normalization for *cylinders*)
$\zeta = \xi J^{-1/2}$ (another useful normalization for *spheres*)
$\zeta = \xi J^{-1}$ (another useful normalization for *cylinders*)
$L =$ angular momentum
$l =$ mean free path of ions
$\iota = I_i(m_i/2ZkT_e)^{1/2}/(\pi r_p{}^2 n_0)$ (normalized ion current in LAM's theory, for *spheres*)

$\iota = I_i(m_i/2ZkT_e)^{1/2}/2r_p n_0$ (normalized ion current in LAM's theory, for *cylinders*)
ι_B = normalized BOHM current, a function of β only
$I_B = \pi r_p^2 n_0 \iota_B (2ZkT_e/m_i)^{1/2}$ (BOHM current to *sphere*, valid for $\xi_p \to \infty$)
$I_B = 2r_p n_0 \iota_B (2ZkT_e/m_i)^{1/2}$ (BOHM current to *cylinder*, valid for $\xi_p \to \infty$)
$I_{e0} = n_0(kT_e/2\pi m_e)^{1/2}$
$\tau = \iota/\iota_B = I_i/I_B$ (a ratio expressing the increase in ion current over the BOHM value, due to finite sheath thickness)
$\Lambda_s(\tau)$, $F(T)$ = functions used in LAM's theory for *spheres*
$\Lambda_c(\tau)$, $G(\psi)$ = functions used in LAM's theory for *cylinders.*

3. FORMULAE AND GRAPHS

For $\beta = 0$ we have used the following equation (ALLEN *et al.*, 1957) for a *spherical probe:*

$$\frac{\mathrm{d}}{\mathrm{d}\xi}\left(\xi^2 \frac{\mathrm{d}\eta}{\mathrm{d}\xi}\right) - J\eta^{-1/2} + \xi^2 \mathrm{e}^{-\eta} = 0. \tag{1}$$

The results for the potential distribution $\eta(\xi)$ for various values of J are shown in

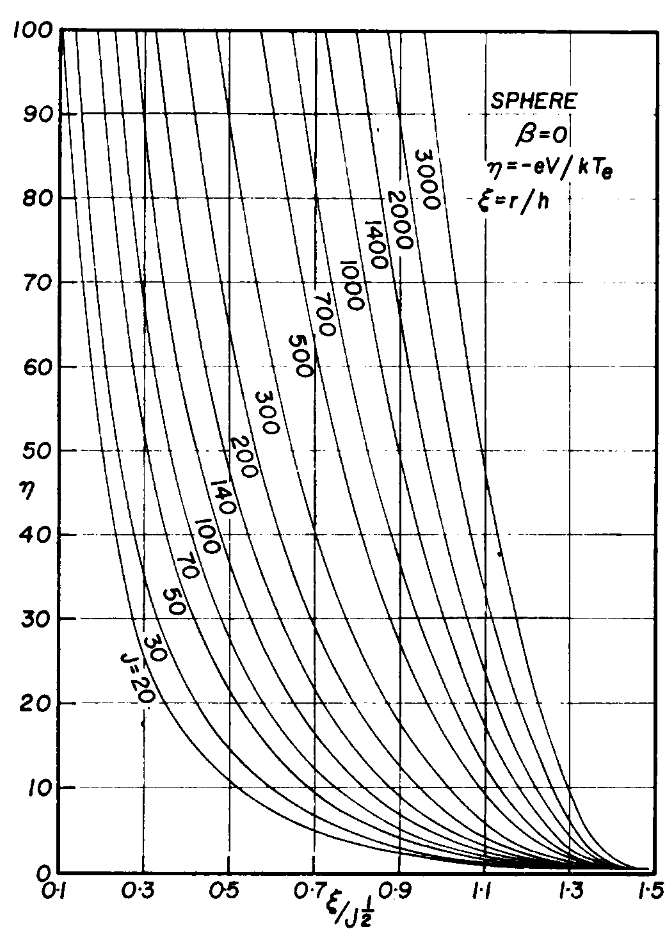

FIG. 1

Fig. 1, where for convenience of presentation we have plotted η vs. the variable $\zeta = \xi J^{-1/2}$. In terms of ζ, equation (1) can be written

$$\frac{1}{J}\frac{\mathrm{d}}{\mathrm{d}\zeta}\left(\zeta^2 \frac{\mathrm{d}\eta}{\mathrm{d}\zeta}\right) - \eta^{-1/2} + \zeta^2 \mathrm{e}^{-\eta} = 0, \tag{2}$$

so that the quasi-neutral solution is the same for all J. A log–log plot of $\eta(\xi)$ is given in Fig. 2 for easier reading at the extremes of the range of ξ. The log ξ–log J cross-plot

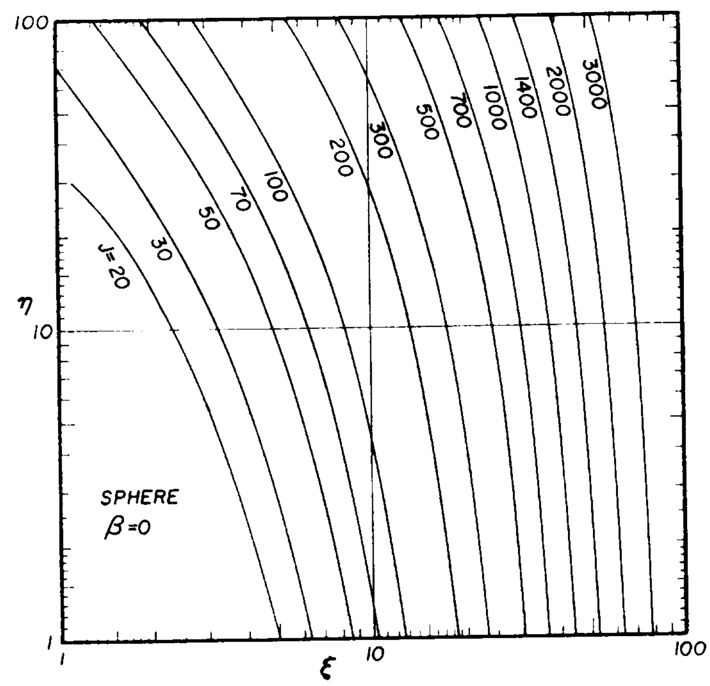

100
10
1
η
ξ
100
J=20
30
50
70
100
200
300
500
700
1000
1400
2000
3000
SPHERE
β=0

FIG. 2

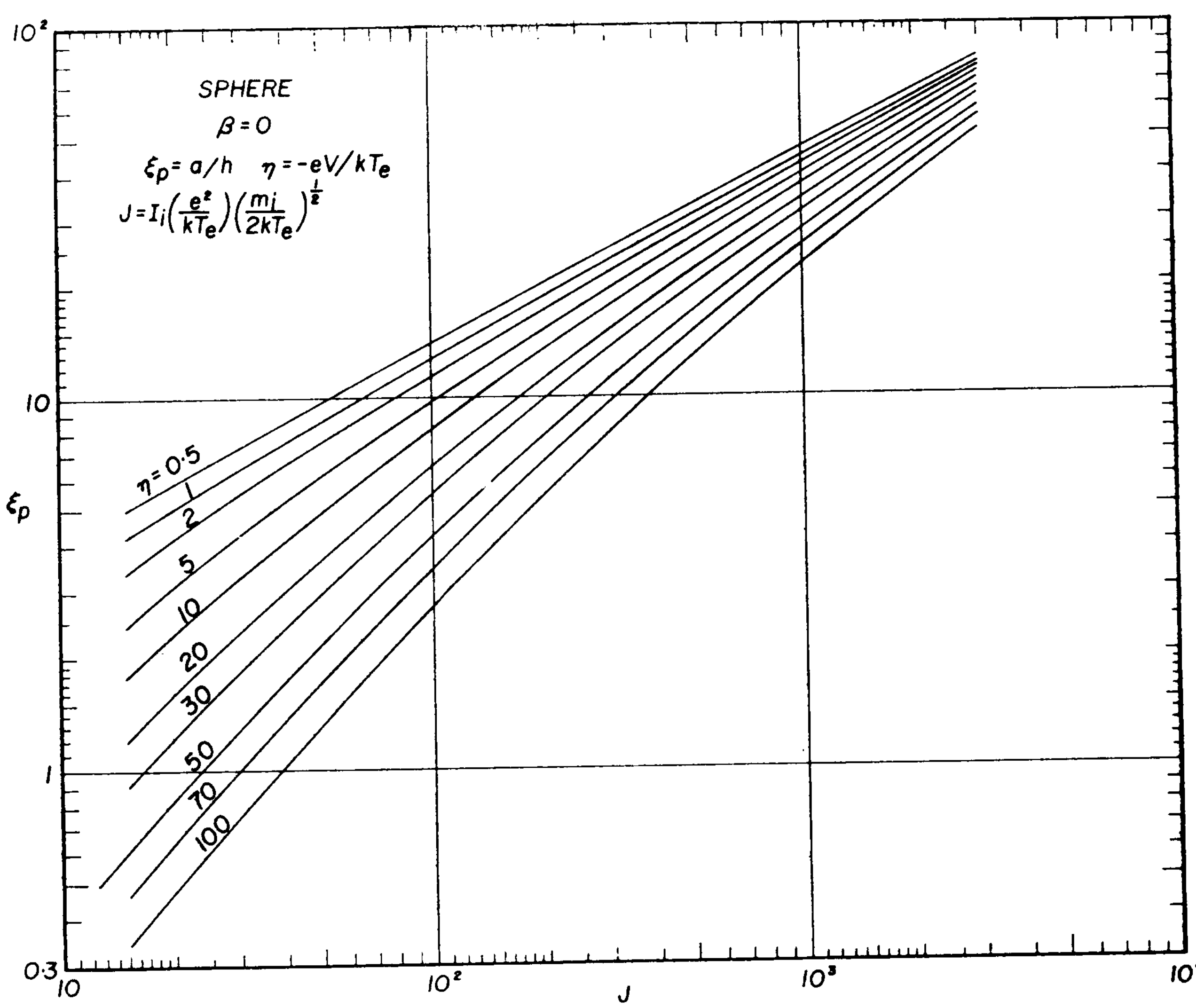

SPHERE
β = 0
ξp = a/h   η = -eV/kTe
J = Ii(e²/kTe)(mi/2kTe)^½
10²
10
1
0·3
ξp
10
10²
10³
10⁴
J
η = 0·5
1
2
5
10
20
30
50
70
100

FIG. 3

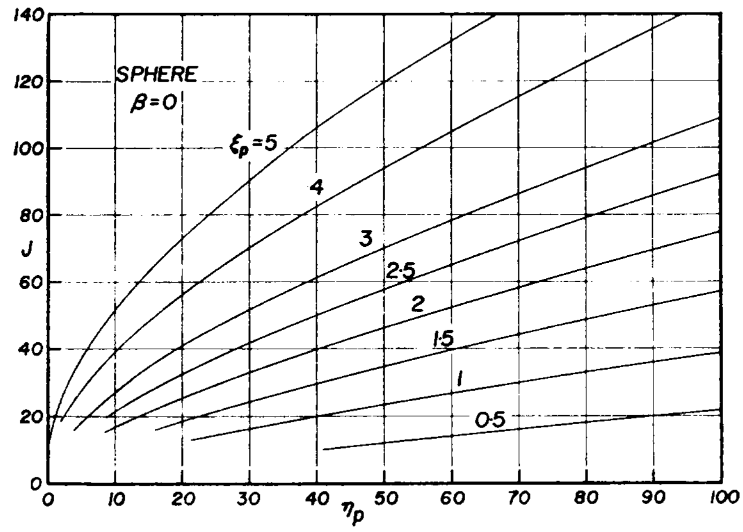
SPHERE
β=0
ξp=5
4
3
2·5
2
1·5
1
0·5
J
ηp

FIG. 4(a)

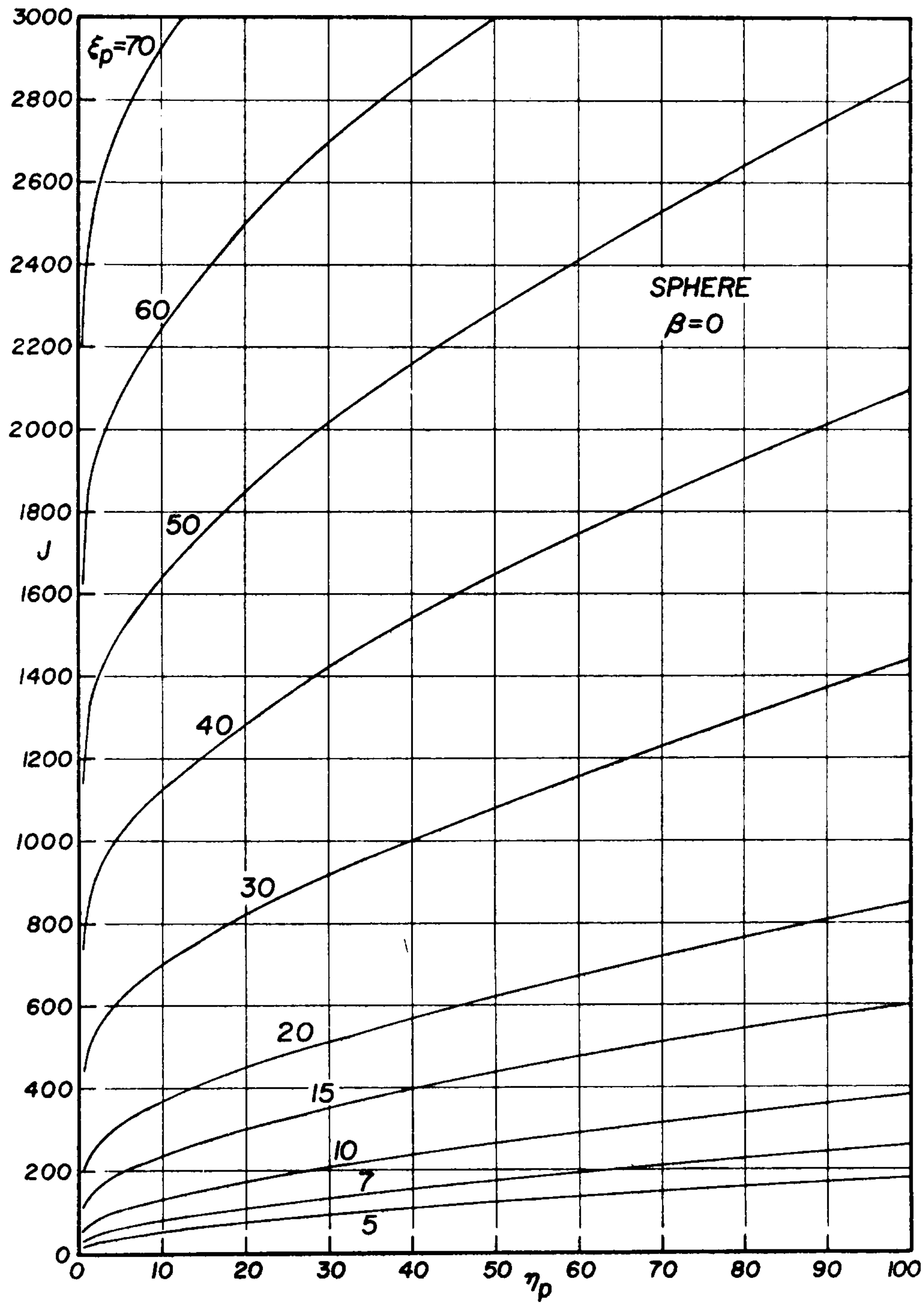
ξp=70
60
50
40
30
20
15
10
7
5
SPHERE
β=0
J
ηp

FIG. 4(b)

of Fig. 3 is used for interpolating in J to obtain the probe characteristics $J(\eta_p)$. The latter are shown for various ξ_p on a linear scale in Figs. 4(a) and 4(b) and on a logarithmic scale in Fig. 5. From Fig. 5 one can see the range in which J varies as $\eta_p^{1/2}$. To find the plasma density, one computes J from the experimental data, using a known value of kT_e, and places the points on Fig. 4. The value of ξ_p is then obtained,

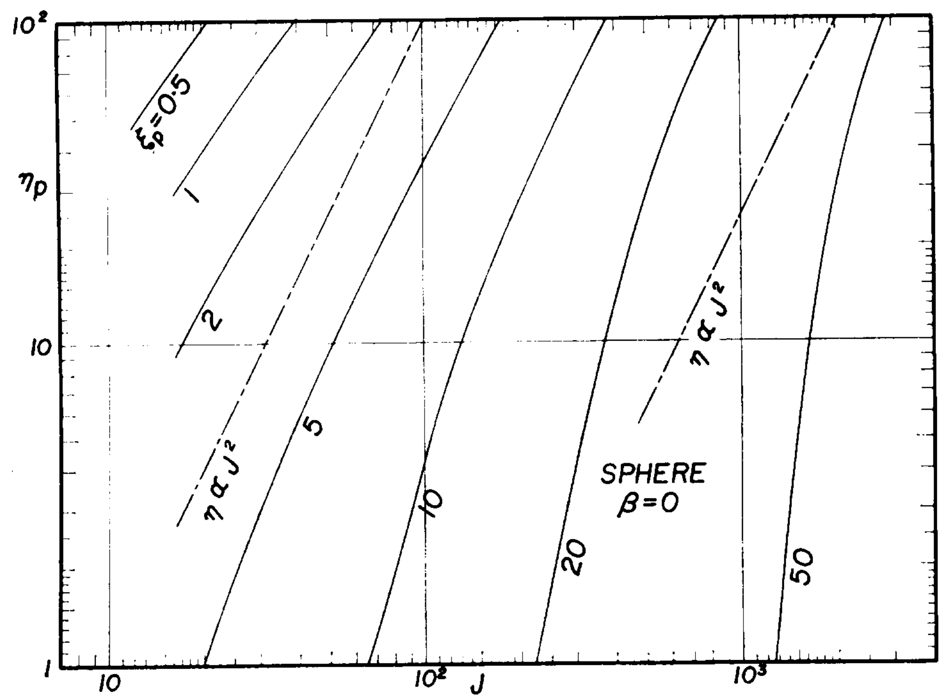

FIG. 5

from which n_0 can be computed. From the curves $\eta(\xi)$ the reader may make whatever cross-plots he wishes if the ones presented here are not convenient.

For $\beta = 0$ we have used the following equation for a *cylindrical probe:*

$$\frac{d}{d\xi}\left(\xi\frac{d\eta}{d\xi}\right) - J\eta^{-1/2} + \xi e^{-\eta} = 0. \tag{3}$$

In terms of $\zeta = \xi J^{-1}$, this reads

$$\frac{1}{J^2}\frac{d}{d\zeta}\left(\zeta\frac{d\eta}{d\zeta}\right) - \eta^{-1/2} + \zeta e^{-\eta} = 0. \tag{4}$$

These equations are valid if the distribution of angular momenta L at ∞ is a delta function around $L = 0$. In practice the collisionless equations are valid only up to a mean free path l, and the validity condition can be written:

$$\frac{-E_i}{eV_p} \ll \frac{r_p{}^2}{l^2}. \tag{5}$$

The potential distribution $\eta(\zeta)$ is shown in Fig. 6. A log–log plot of $\eta(\xi)$ is given in Fig. 7. The log ξ–log $J\xi$ cross-plot is given in Fig. 8. From this one obtains the probe characteristics $J\xi_p(\eta_p)$ for various ξ_p shown linearly in Figs. 9(a), 9(b), 9(c) and logarithmically in Fig. 10. From the latter one can see the range in which $J\xi_p$ varies as $\eta_p^{1/2}$. The quantity $J\xi_p$ is used because it is independent of n_0. To find the plasma density when kT_e is known, one computes $J\xi_p$ from the experimental data and places the points on Fig. 9. A value of ξ_p is then obtained, from which n_0 is easily calculated.

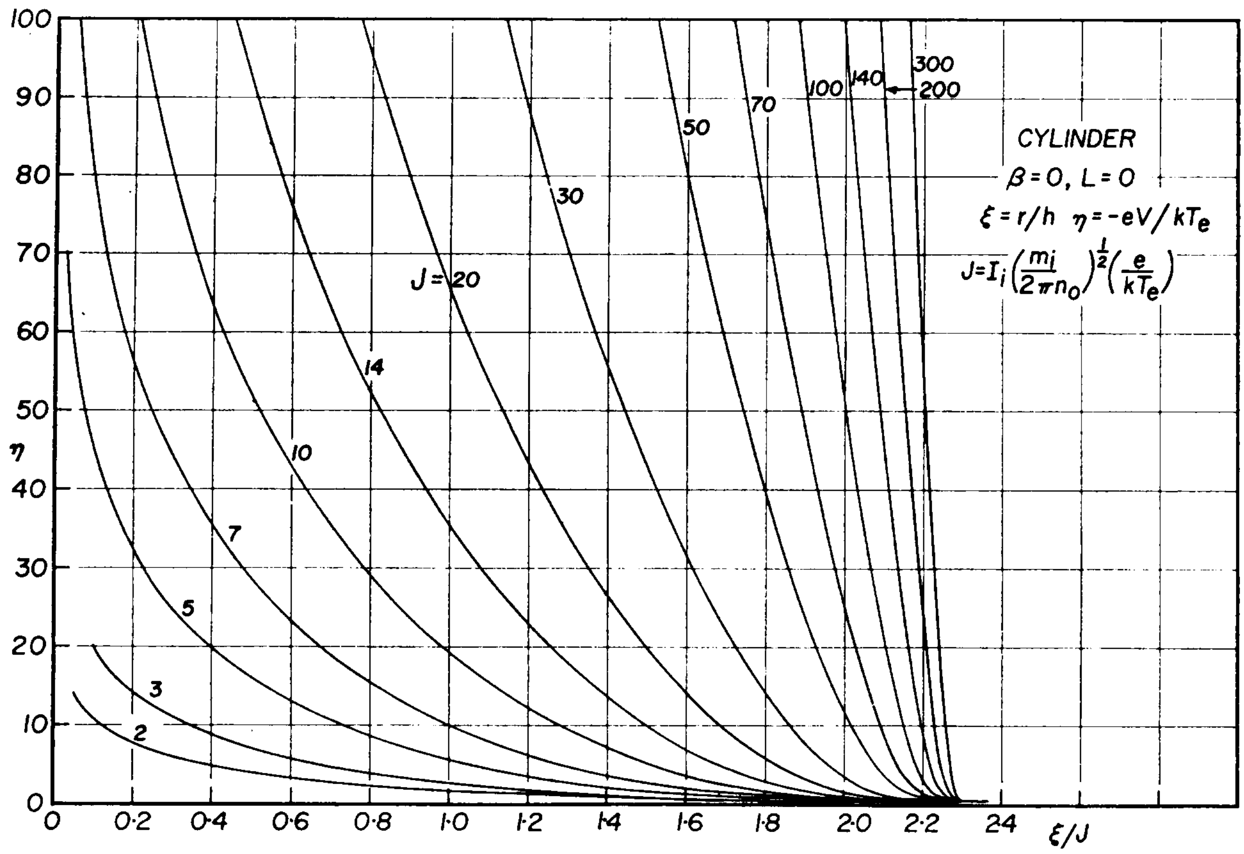

FIG. 6

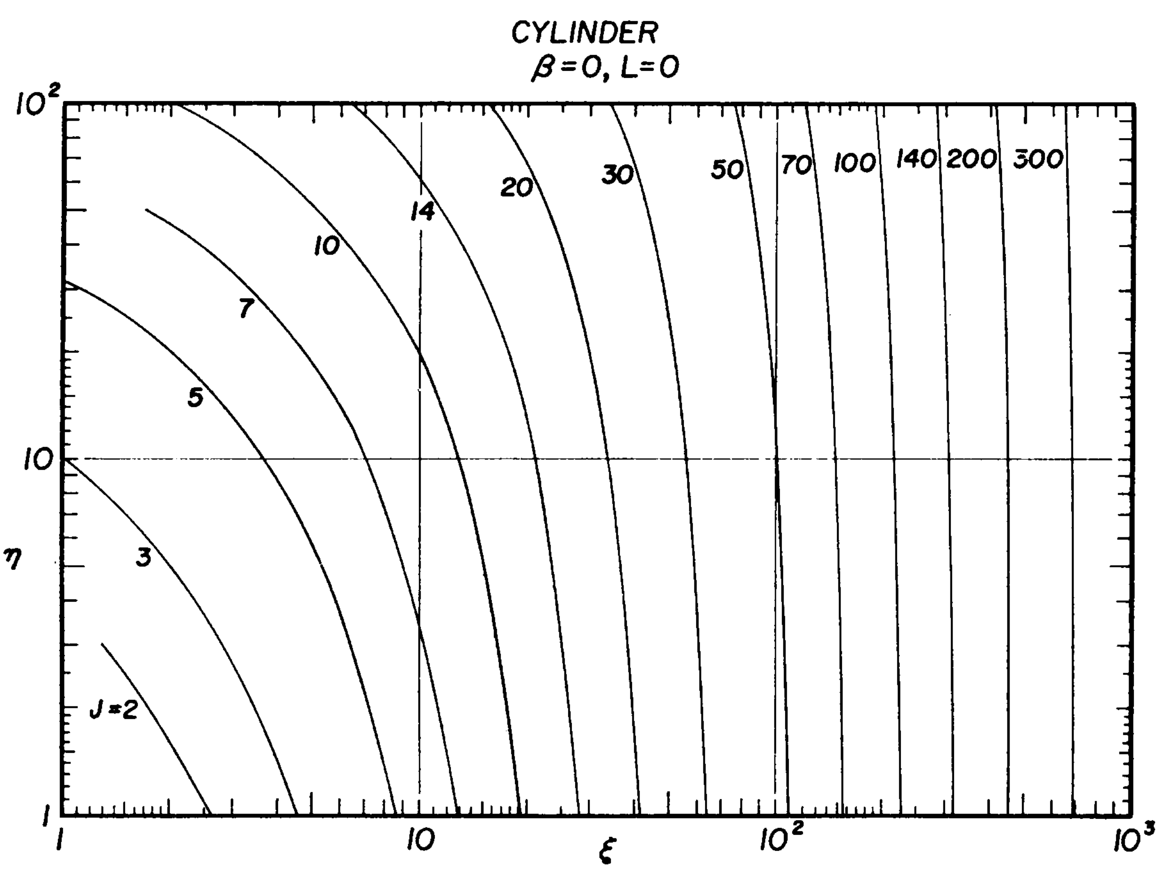

FIG. 7

For finite β we have used the following equation (BERNSTEIN and RABINOWITZ) for a *spherical probe*:

$$\frac{1}{\xi^2}\frac{\mathrm{d}}{\mathrm{d}\xi}\left(\xi^2\frac{\mathrm{d}\eta}{\mathrm{d}\xi}\right) = \frac{1}{2}\left(1+\frac{\eta}{\beta}\right)^{1/2} \pm \frac{1}{2}\left[1+\frac{\eta}{\beta}-\frac{4J}{\beta^{1/2}\xi^2}\right]^{1/2} - \mathrm{e}^{-\eta}, \tag{6}$$

where the plus sign is used for the exterior region $\xi \geq \xi_0$ and the minus sign for the interior region $\xi \leq \xi_0$. The absorption radius ξ_0 occurs when the square bracket vanishes.

The potential profiles $\eta(\xi)$ for various J have been taken from the computations of BERNSTEIN and RABINOWITZ and are shown in Figs. 11(a), 11(b), 11(c) for $\beta = 0{\cdot}01$, $0{\cdot}05$, and $0{\cdot}1$, respectively. The cross-plots $J(\eta)_p$ for various ξ_p are shown

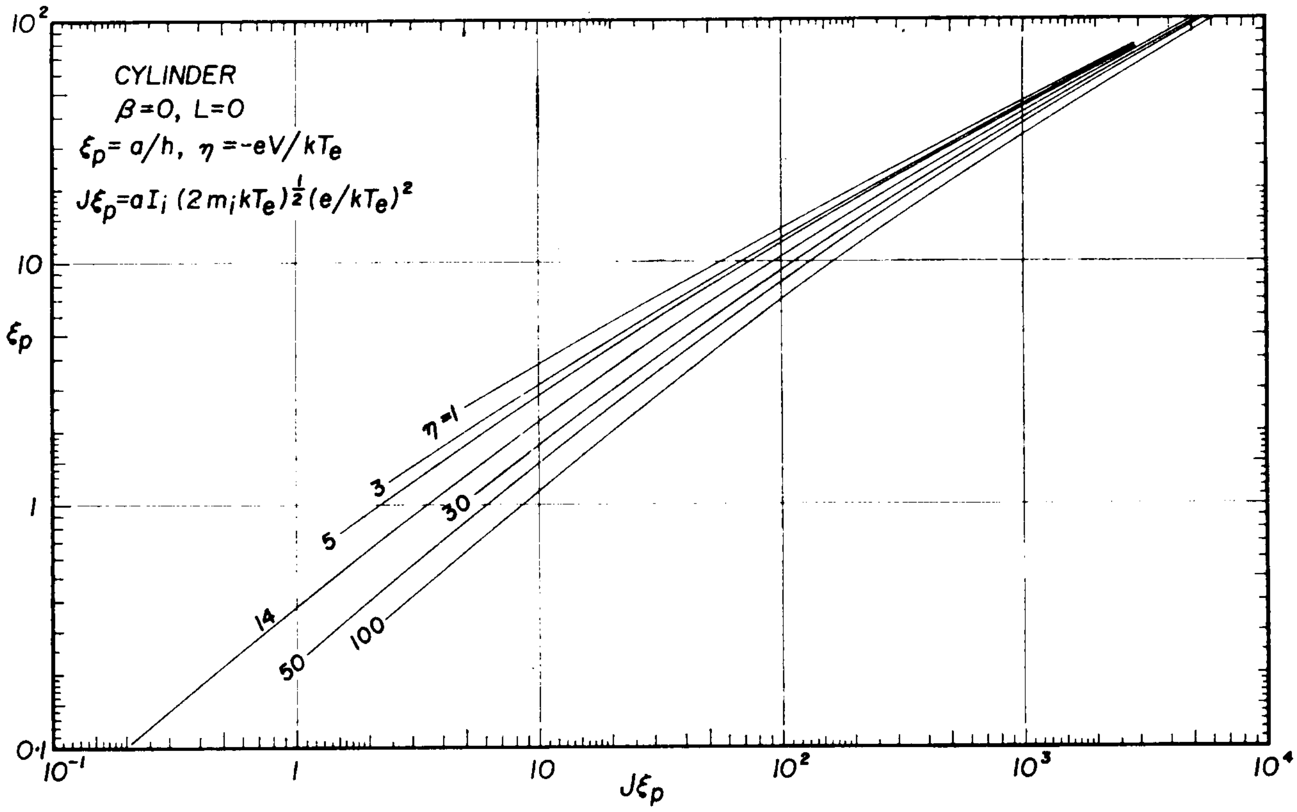

FIG. 8

in Figs. 12(a), 12(b), 12(c). These are the probe characteristics. To show the dependence on β, we have plotted in Fig. 13 the probe characteristics for $\xi_p = 10$ and various values of β, including $\beta = 0$ from Fig. 4. In general, the dependence on β is small for large ξ_p and becomes measurable for $\xi_p \lessdot 10$. A log–log plot of $J(\eta_p)$ for various

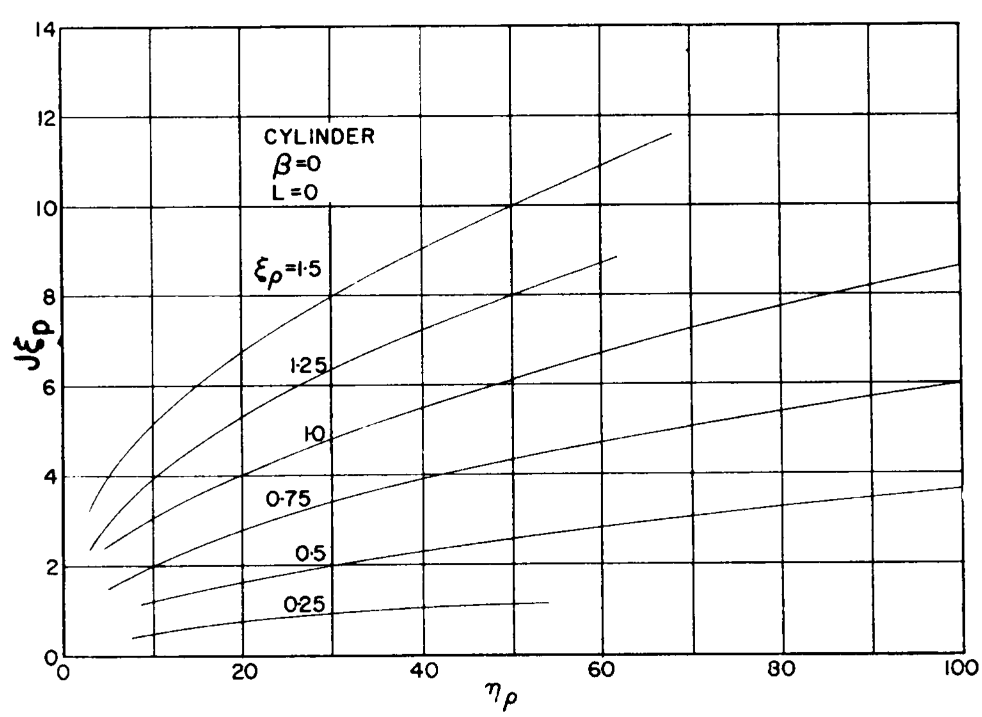

FIG. 9(a)

ξ_p is given in Fig. 14 for $\beta = 0{\cdot}1$ to show the range in which J varies approximately as $\eta_p^{1/2}$. The plasma density is found the same way as in the $\beta = 0$ case, only an approximate value of β must now be chosen. These results are valid for a monoenergetic, isotropic ion distribution but because of the insensitivity to β for $\beta \ll 1$ they may be

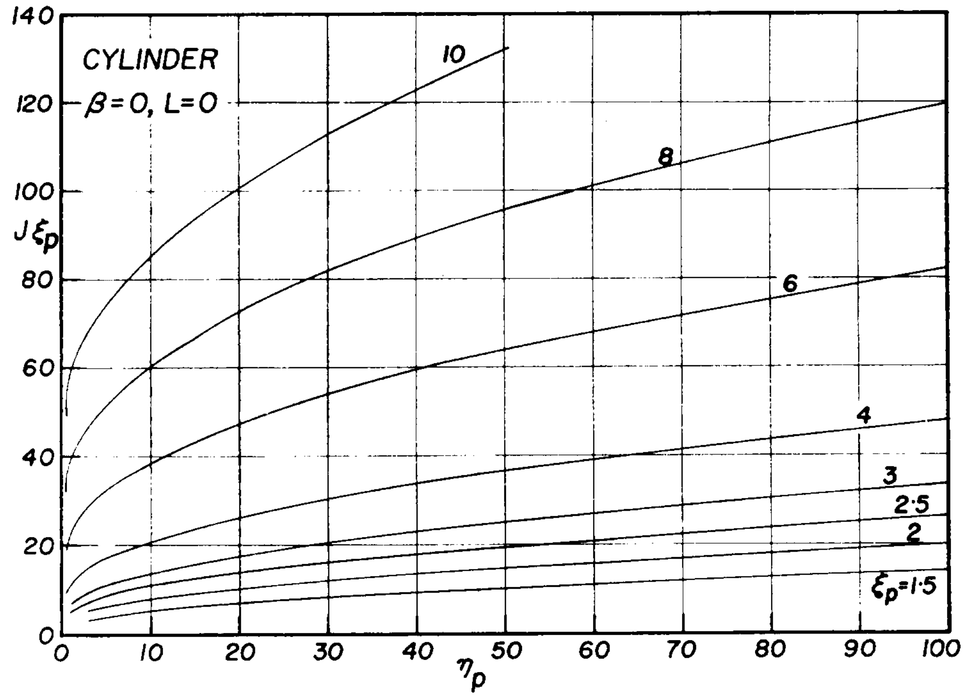
CYLINDER
β=0, L=0
Jξp
ηp
10
8
6
4
3
2·5
2
ξp=1·5
0
10
20
30
40
50
60
70
80
90
100
120
140

FIG. 9(b)

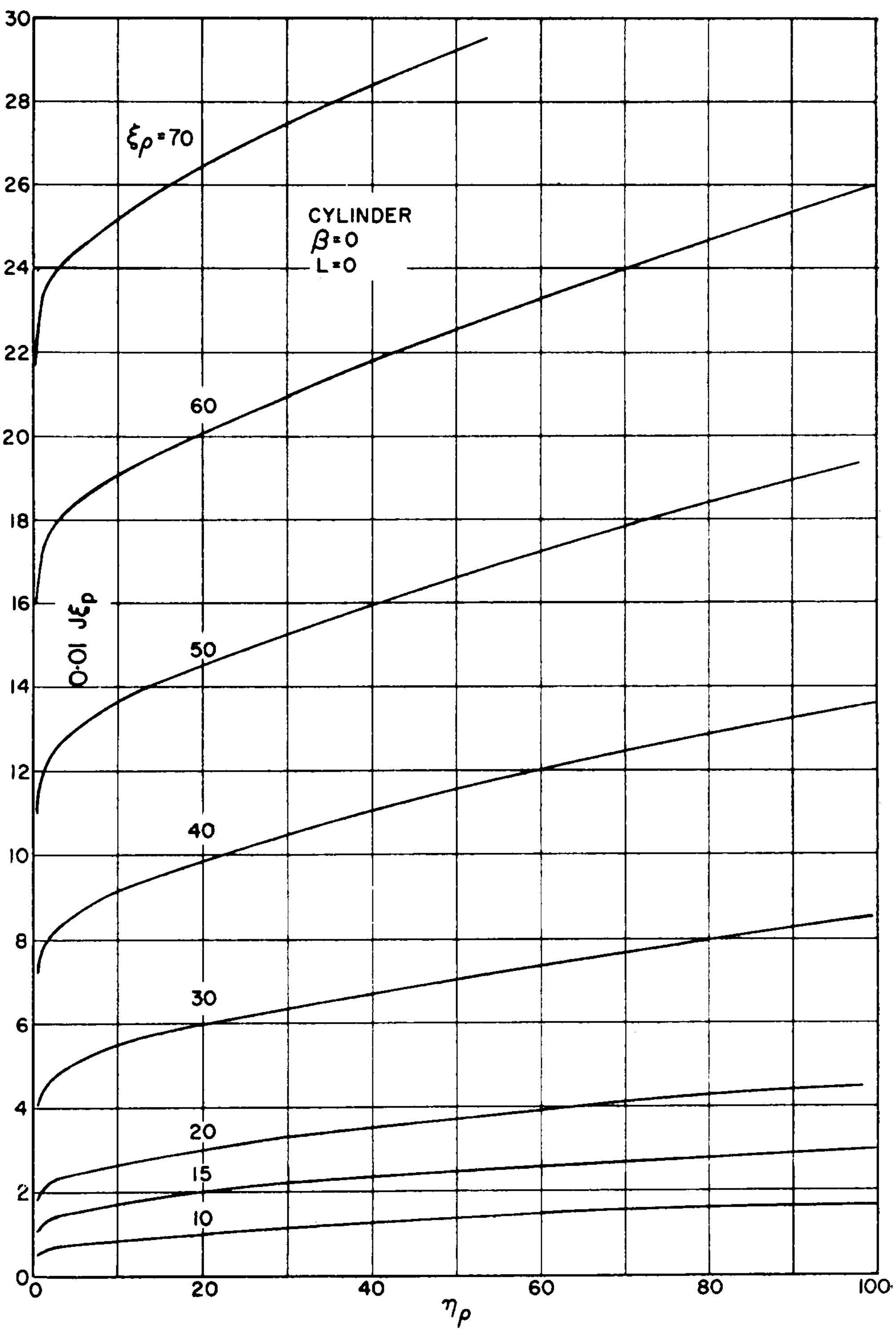
ξρ=70
CYLINDER
β=0
L=0
60
50
40
30
20
15
10
0·01 Jξp
ηρ

FIG. 9(c)

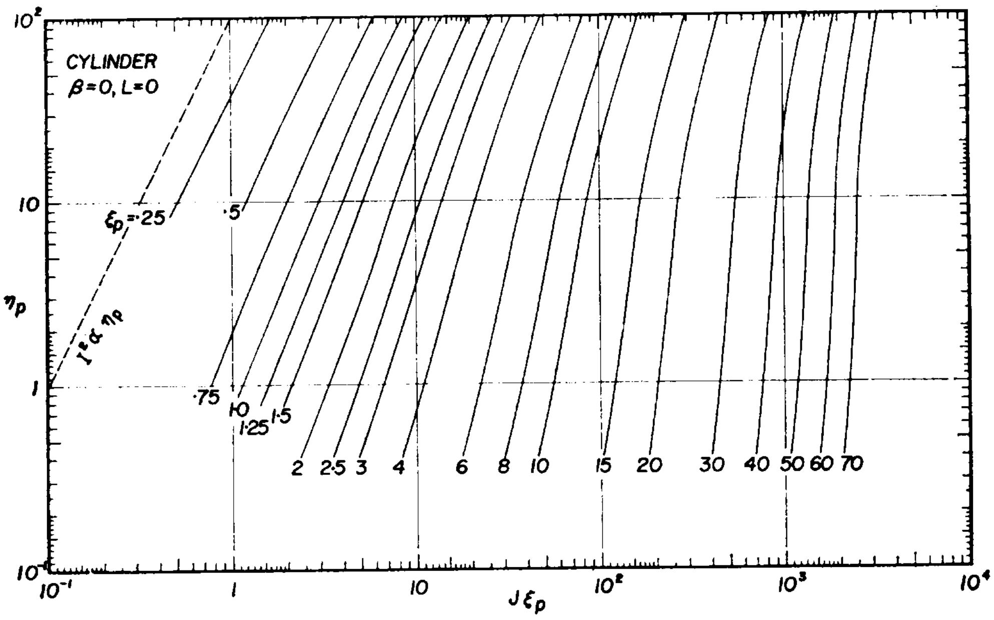

FIG. 10

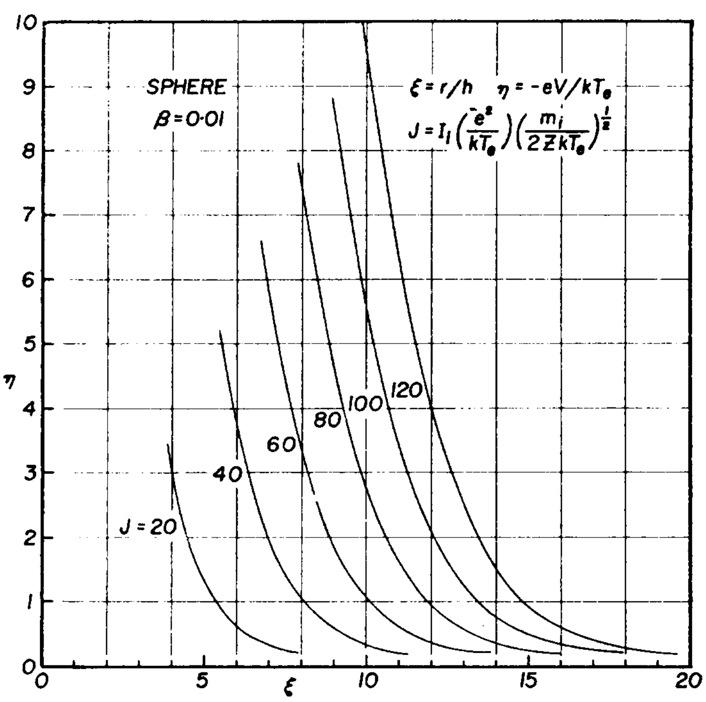

FIG. 11(a)

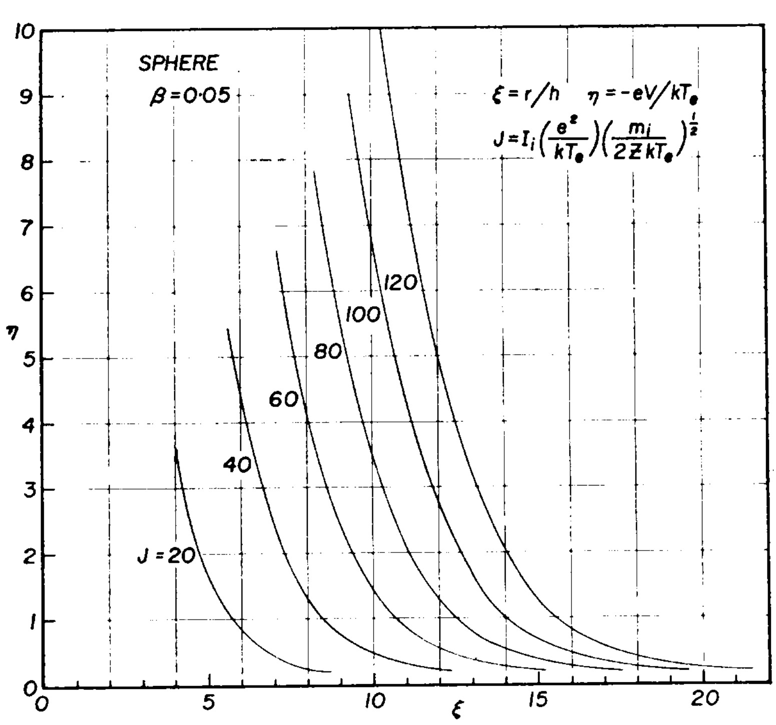

FIG. 11(b)

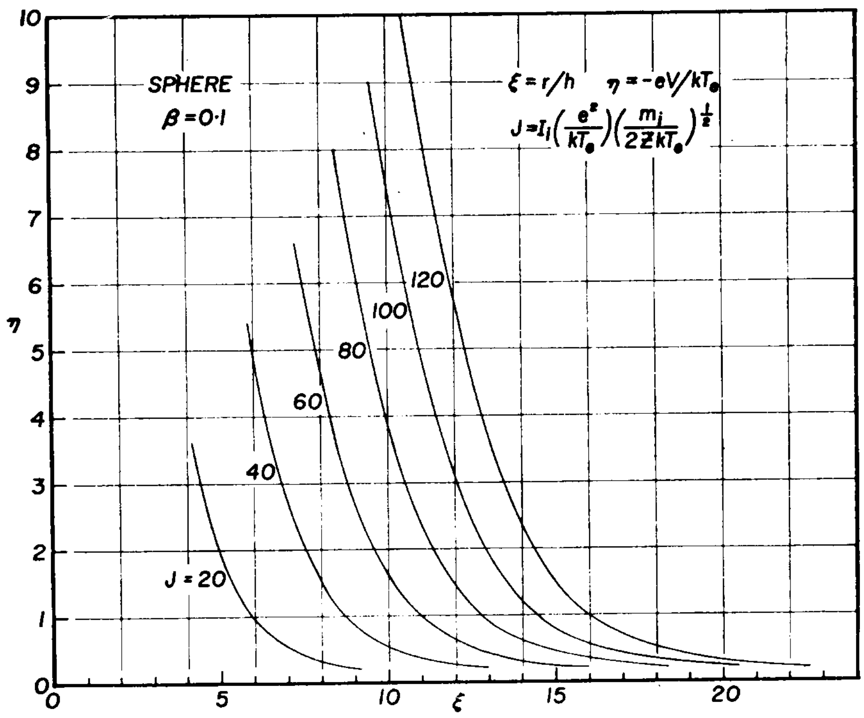

FIG. 11(c)

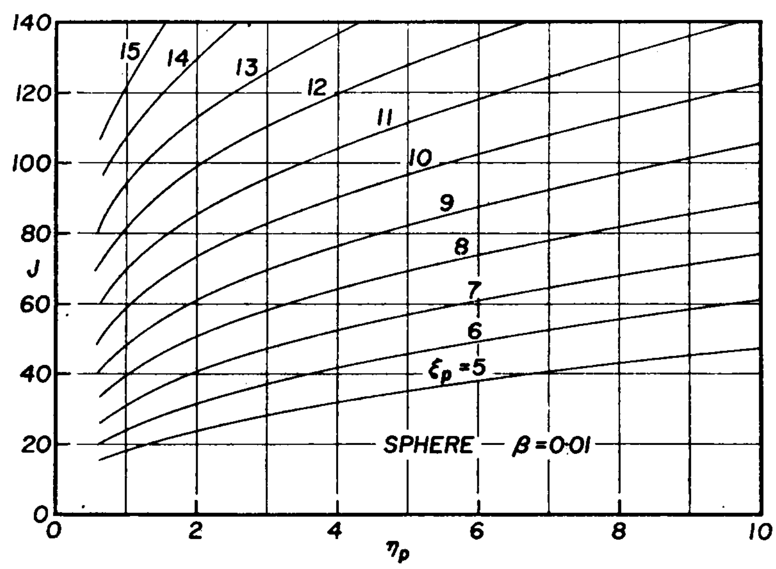

FIG. 12(a)

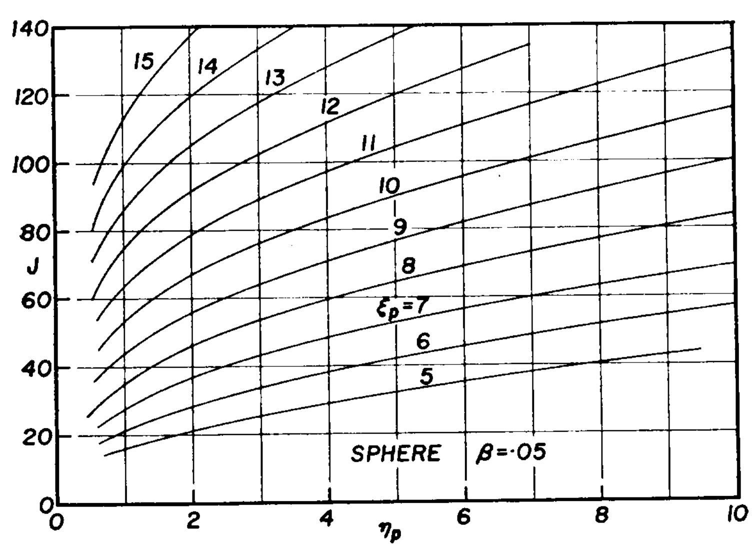

FIG. 12(b)

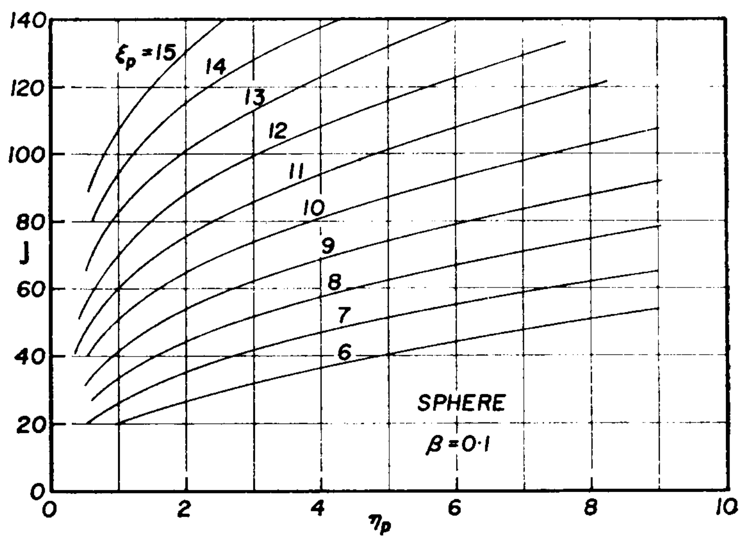

FIG. 12(c)

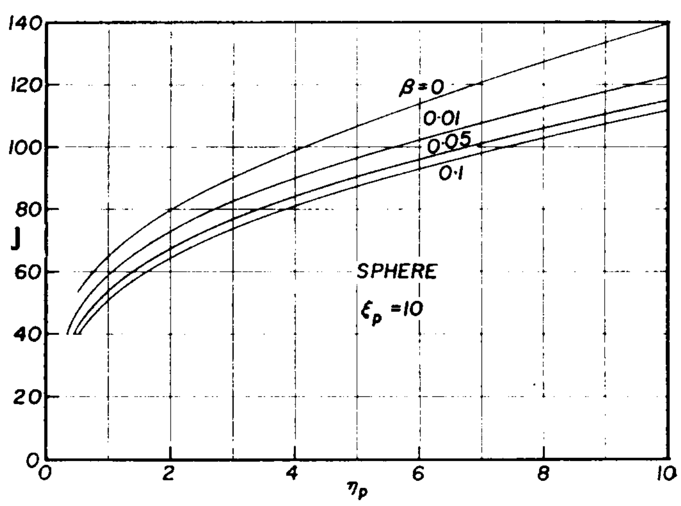

FIG. 13

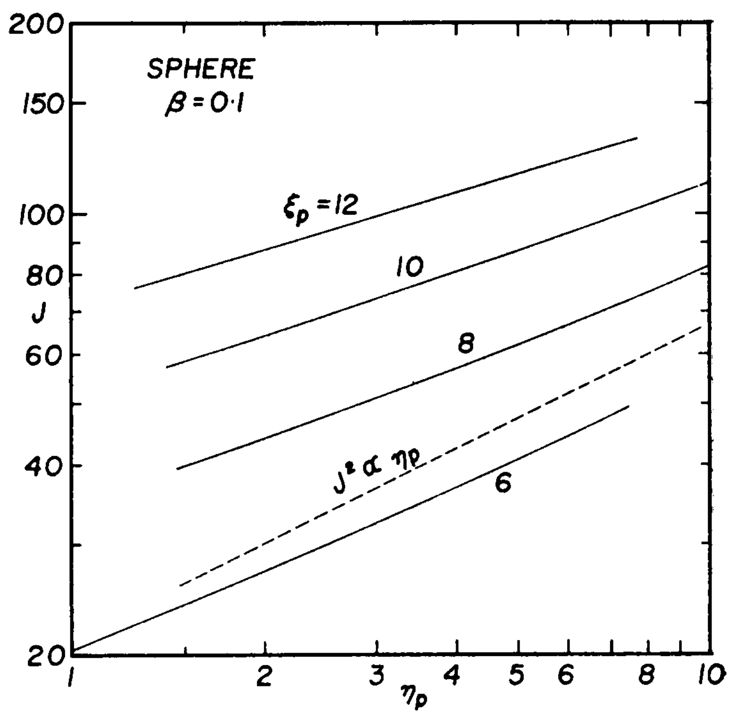

FIG. 14

applied to a Maxwellian distribution of such a temperature that the random current is kept the same; thus the equivalent ion temperature is

$$\begin{aligned} &\text{Spheres:} \quad kT_i = \frac{\pi}{4} E_i = \frac{\pi}{4} \beta Z k T_e. \\ &\text{Cylinders:} \quad kT_i = \frac{4}{\pi} E_i = \frac{4}{\pi} \beta Z k T_e. \end{aligned} \tag{7}$$

For finite β we have used the following equation (Bernstein and Rabinowitz) for a cylindrical probe:

$$\frac{1}{\xi}\frac{\mathrm{d}}{\mathrm{d}\xi}\left(\xi\frac{\mathrm{d}\eta}{\mathrm{d}\xi}\right) = \begin{Bmatrix}1\\0\end{Bmatrix} \mp \frac{1}{\pi}\sin^{-1}\left[\frac{\pi J}{\xi(\beta+\eta)^{1/2}}\right] - \mathrm{e}^{-\eta}, \tag{8}$$

where the top choice is for $\xi \geq \xi_0$ and the bottom choice is for $\xi \leq \xi_0$. The absorption radius ξ_0 occurs when the square bracket is unity. The data of Bernstein and Rabinowitz for the potential profiles $\eta(\xi)$ for various β and J are plotted in Figs. 15(a–f) to show the shape of $\eta(\xi)$ and the dependence on β. New

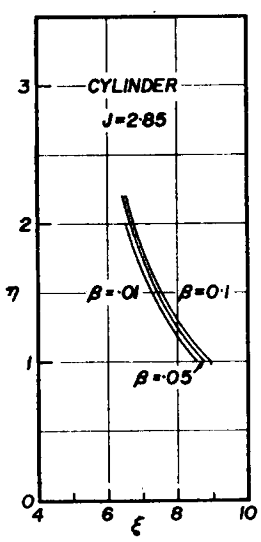

Fig. 15(a)

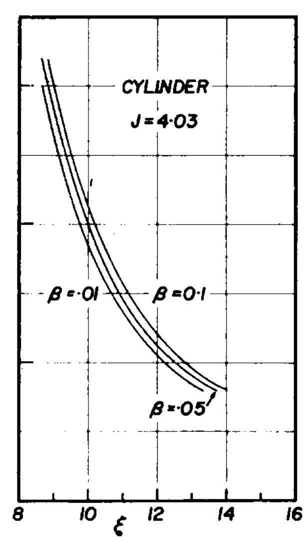

Fig. 15(b)

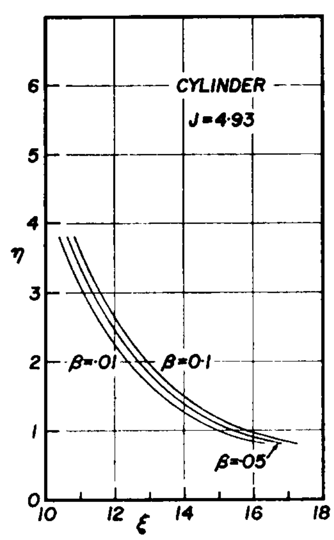

Fig. 15(c)

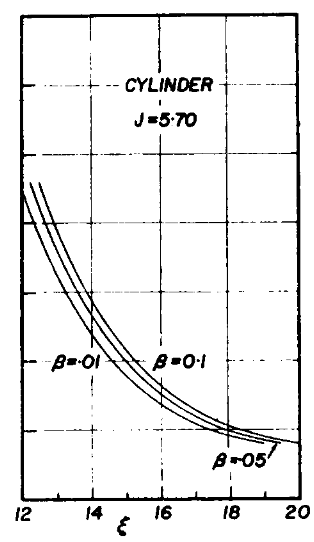

Fig. 15(d)

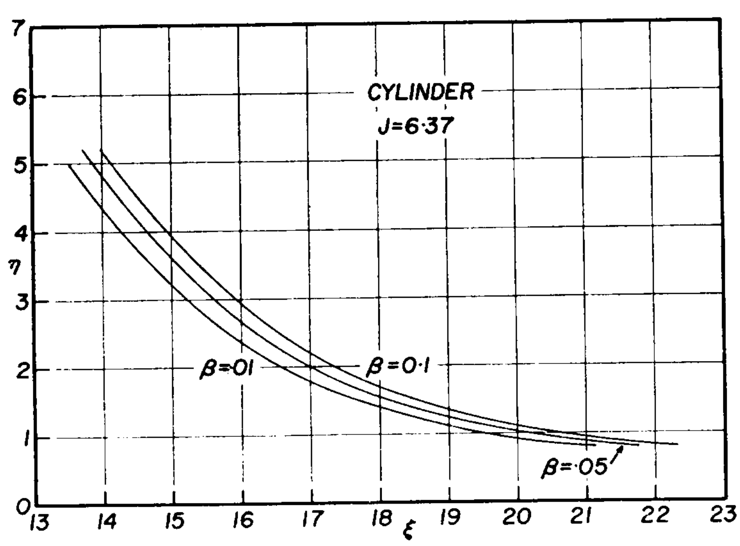

Fig. 15(e)

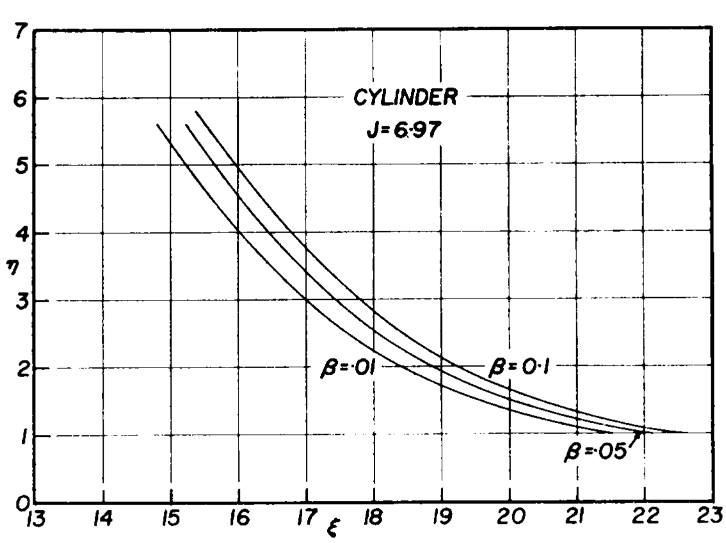

Fig. 15(f)

computations for $\eta(\xi)$ at various J for $\beta = 0{\cdot}01$, $0{\cdot}03$ and $0{\cdot}1$ are shown in Figs. 16(a–c) on log-log plots. The behaviour of a typical quasi-neutral curve is also shown. From Fig. 16 one obtains by cross-plotting the probe characteristics $J\xi_p(\eta)_p$

for various values of ξ_p. These are shown in Fig. 17 for $\beta = 0{\cdot}1$; the β-dependence is so small that we have not bothered to plot other values of β. We have plotted $J\xi_p$ rather than J because $J\xi_p$ is independent of n_0; the density can then be determined as in the $\beta = 0$ case. Unfortunately, large values of ξ_p for large η_p could not be

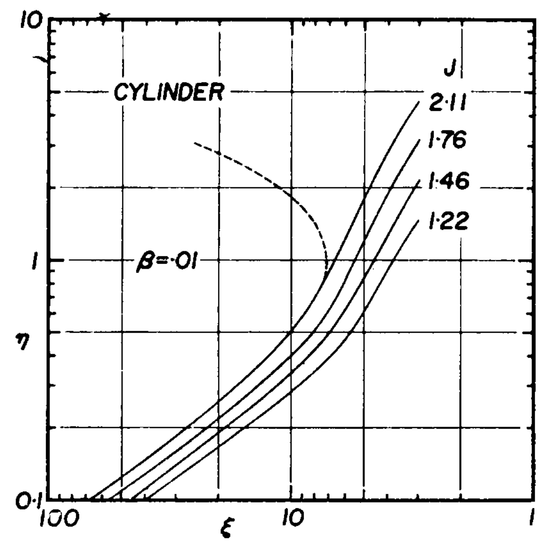

FIG. 16(a)

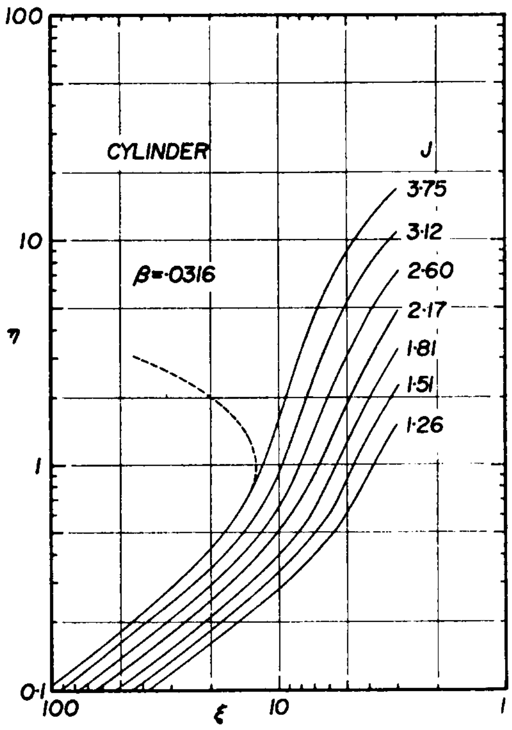

FIG. 16(b)

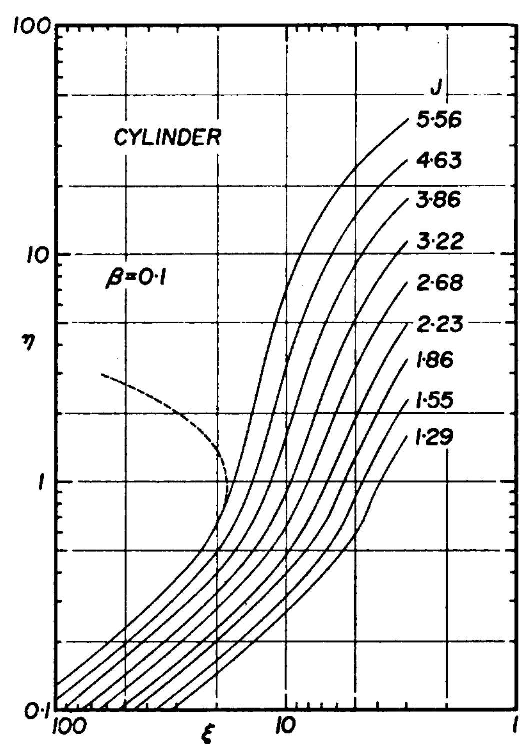

FIG. 16(c)

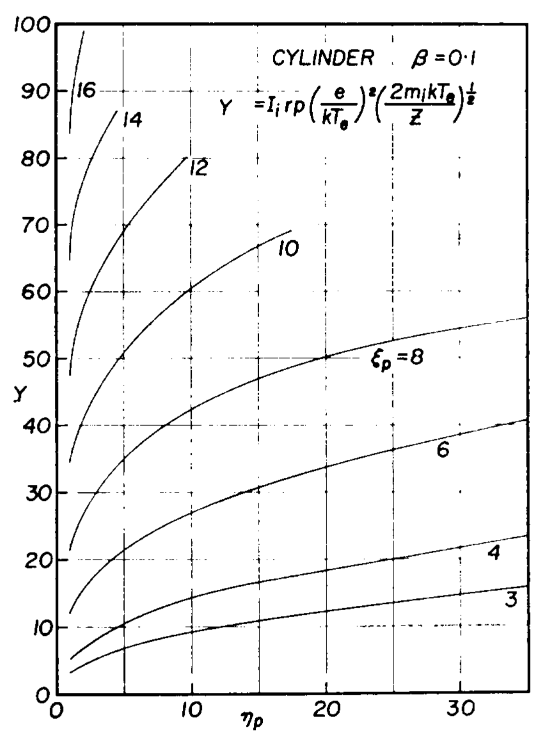

FIG. 17

obtained with the programme we used. In Fig. 18 we show the probe characteristics on a log–log scale to make clear the range in which J varies approximately as $\eta_p^{1/2}$.

Equation (8) is based on the assumption of a distribution of angular momenta L at ∞ which is independent of L. Hence the assumed distribution is not isotropic in the cylindrical case; it is monoenergetic in $E_{i\perp}$ and arbitrary in $E_{i\parallel}$; the projections of the velocities on a plane perpendicular to the probe axis are isotropic. However, because of the insensitivity to β, the present results may also be used for a Maxwellian distribution if $\beta \ll 1$. If one takes the limit of equation (8) as $\beta \to 0$, one does not recover equation (3) for $\beta = 0$ unless the arc sin may be replaced by its argument. The reason for this lies in the indeterminacy of L as $\xi \to \infty$. When the inequality (5) is not satisfied, equation (8) should be used. This problem does not arise for the sphere. We have not computed the $\beta = 0$ case with equation (8); however, for large ξ_p and η_p the difference between equation (3) and (8) should be small.

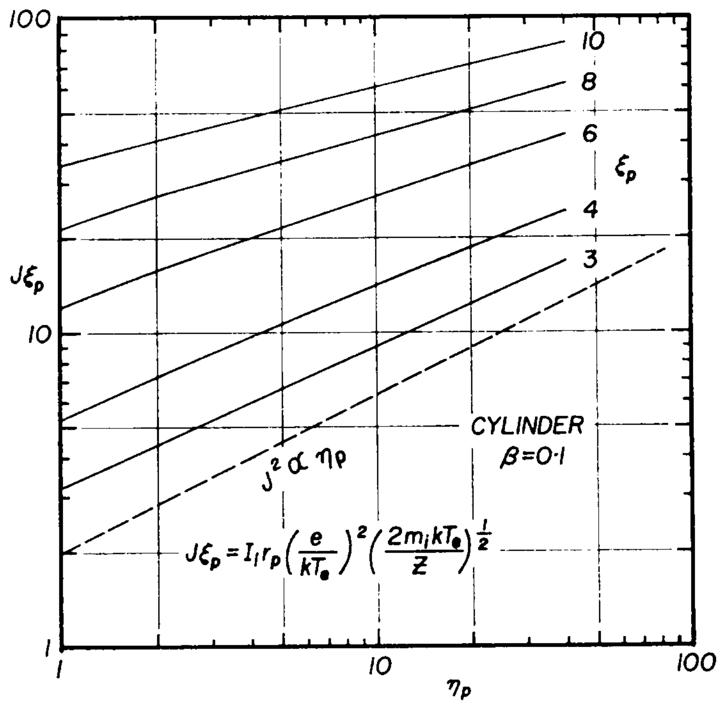

FIG. 18

For large ξ_p the probe characteristics are more easily computed by the method of LAM. For this one uses the LAM diagram of Fig. 19. Suppose r_p, n_0, kT_e, and β are known; then the β-dependent coefficient A of Fig. 19 is found from Fig. 20 for spheres and Fig. 21 for cylinders and $A\xi_p^{4/3}$ is computed. For a given η_p, one follows a path like the dotted one shown in the upper half of Fig. 19 to find I_i/I_B, where I_B is the BOHM current defined in Section 2. The electron component can be found similarly from the lower half of Fig. 19. Strictly speaking, the curves of constant I_{e0}/I_B for each element depend on β; but we have neglected this slight variation. The coefficient A is defined by

$$\begin{aligned} A &= (4/\iota_B)^{2/3} \text{ (spheres)} \\ A &= (\pi/\iota_B)^{2/3} \text{ (cylinders)}, \end{aligned} \tag{9}$$

where ι_B is found from the following transcendental equations:

$$\text{Spheres:} \quad \iota_B = 4e^{-\eta_1}[\tfrac{1}{2}(\eta_1 + \beta)^{-1/2} + \beta^{1/2}e^{-\eta_1}] \tag{10}$$

$$\eta_1 = \tfrac{1}{2} - \beta + [2\beta^{1/2}(\eta_1 + \beta)^{1/2}e^{-\eta_1}] \tag{11}$$

$$\text{Cylinders:} \quad \iota_B = (\eta_1 + \beta)\sin(\pi e^{-\eta_1}) \tag{12}$$

$$\tan(\pi e^{-\eta_1}) = 2(\eta_1 + \beta)\pi e^{-\eta_1}. \tag{13}$$

Values of ι_B and η_1 obtained by hand computation and graphical methods are shown in Figs. 20 and 21.

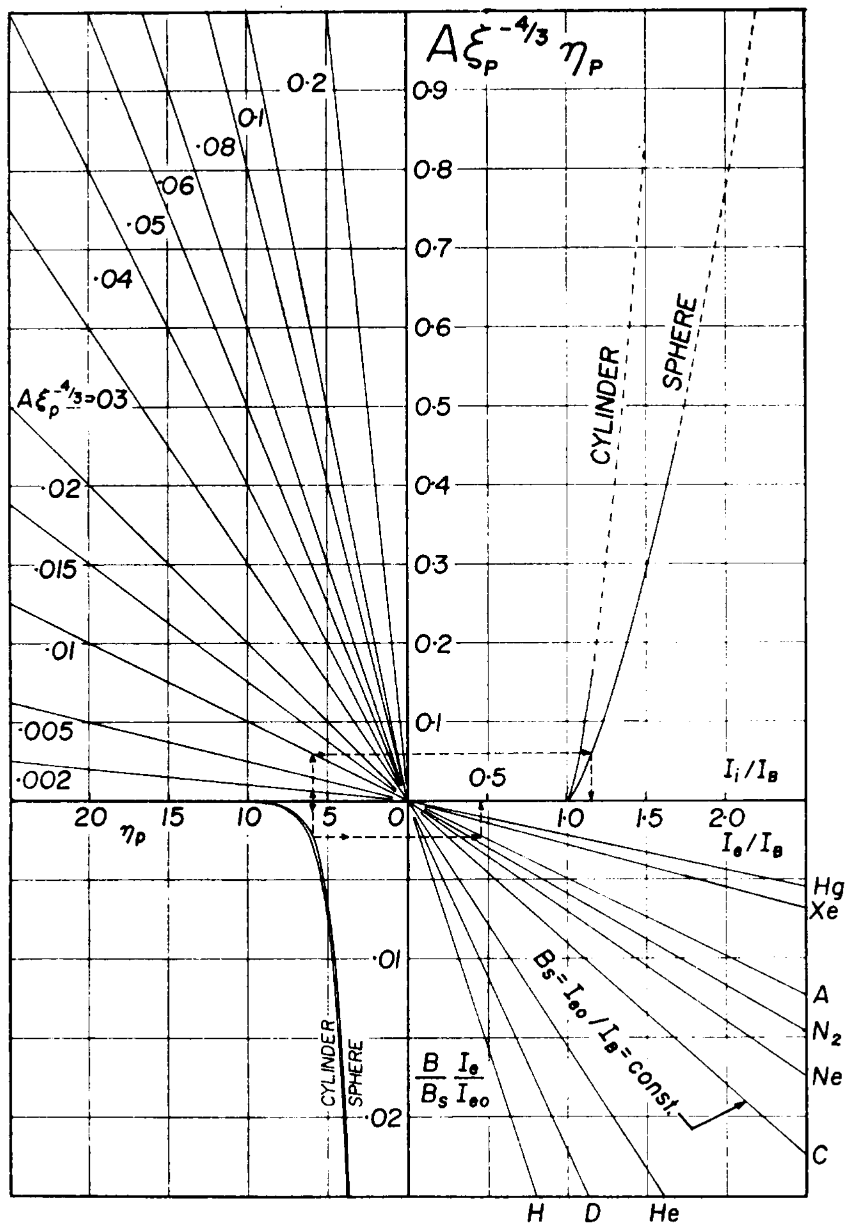
$A\xi_p^{-4/3}$ η_p
CYLINDER
SPHERE
$A\xi_p^{-4/3}$=03
I_i/I_B
I_e/I_B
η_p
$B_s=I_{eo}/I_B$=const.
$\frac{B}{B_s}\frac{I_e}{I_{eo}}$
Hg
Xe
A
N_2
Ne
C
H
D
He

FIG. 19

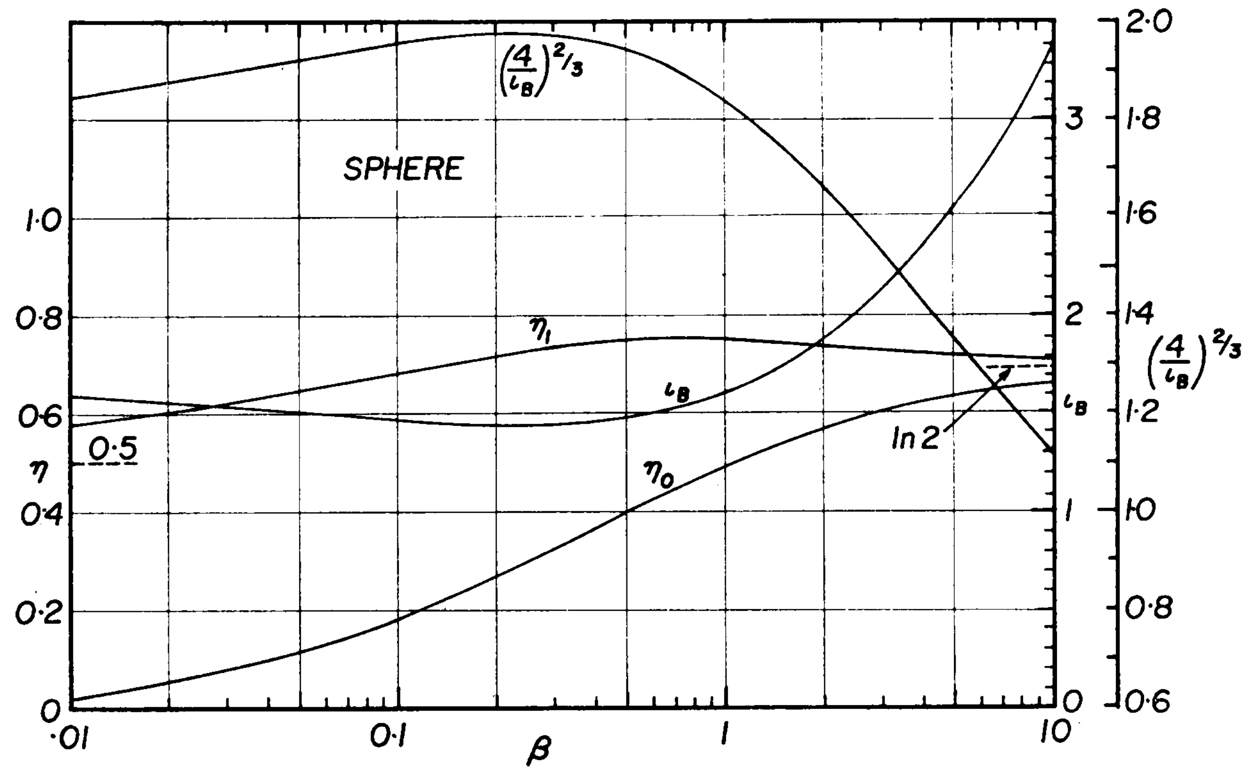
SPHERE
$\left(\frac{4}{\iota_B}\right)^{2/3}$
η_1
ι_B
η_0
ln2
η
β

FIG. 20

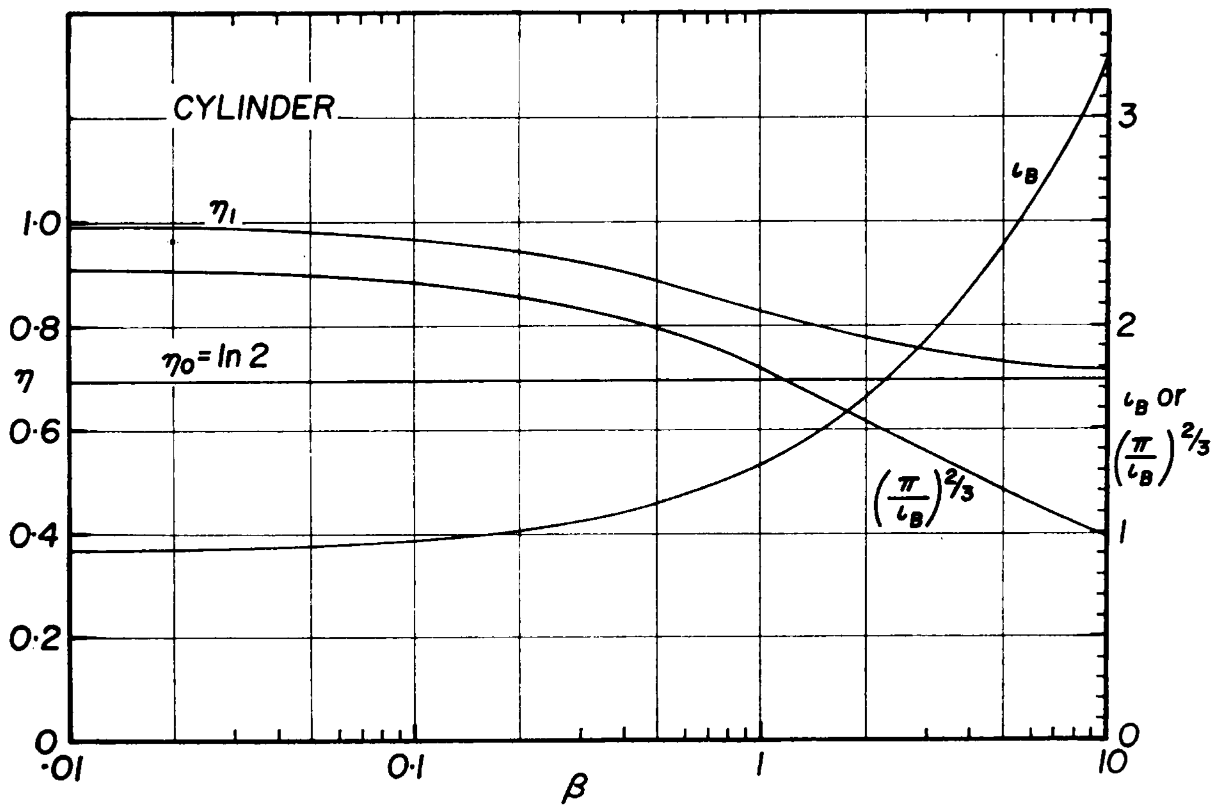

FIG. 21

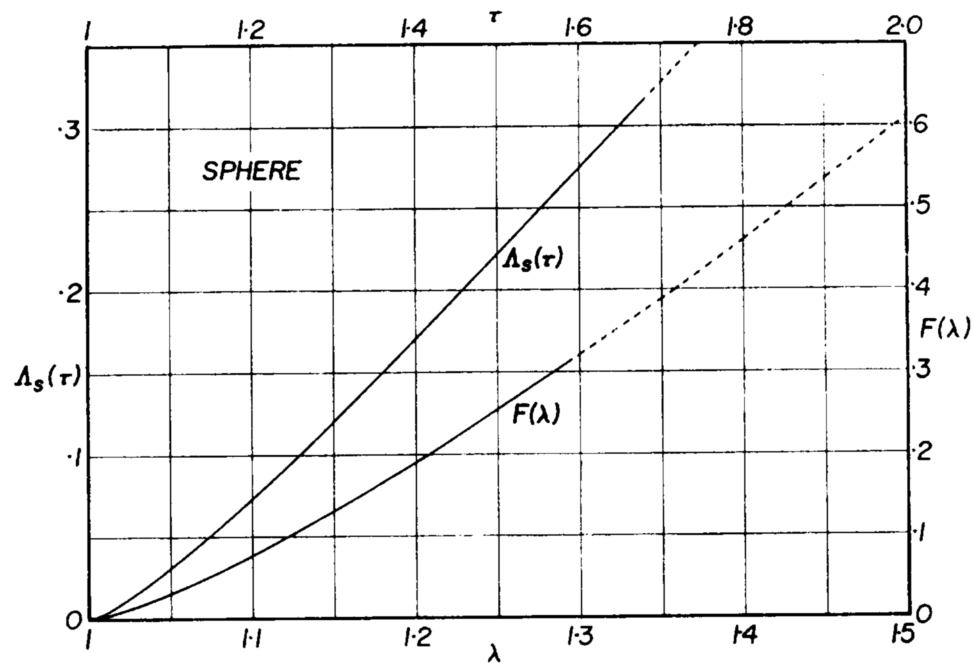

FIG. 22

To determine the plasma density one uses the following formulae (in e.s.u.):

$$\text{Sphere:} \quad \frac{-V_p}{(eI_i)^{2/3}} = \left(\frac{m_i}{2Ze}\right)^{1/3} \Lambda_s(\tau), \tag{14}$$

$$\text{Cylinder:} \quad \frac{-V_p}{(eI_i a)^{2/3}} = \left(\frac{2m_i}{Ze}\right)^{1/3} \Lambda_c(\tau), \tag{15}$$

where

$$\tau = \iota/\iota_B = I_i/I_B. \tag{16}$$

The left-hand side is computed from the experimental data; then, having $\Lambda_s(\tau)$ or $\Lambda_c(\tau)$, one finds τ from Figs. 22, 23 or 24. Knowing τ, one finds I_i from ι_B given in Figs. 20 or 21. The function $\Lambda_s(\tau)$ is defined as

$$\Lambda_s(\tau) = F(\tau^{1/2}), \tag{17}$$

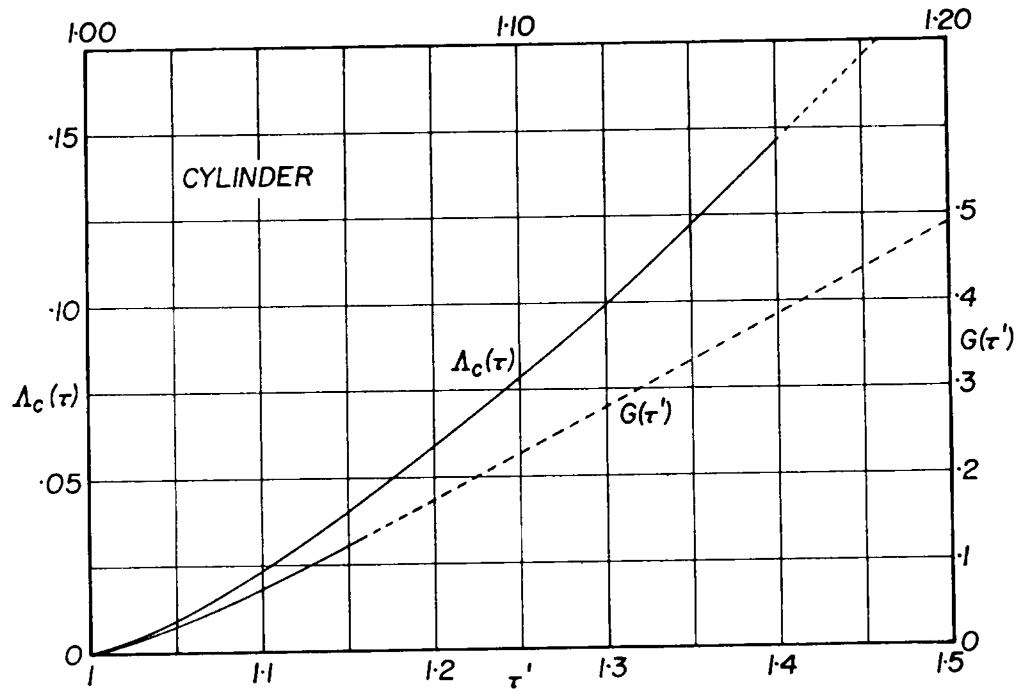

FIG. 23

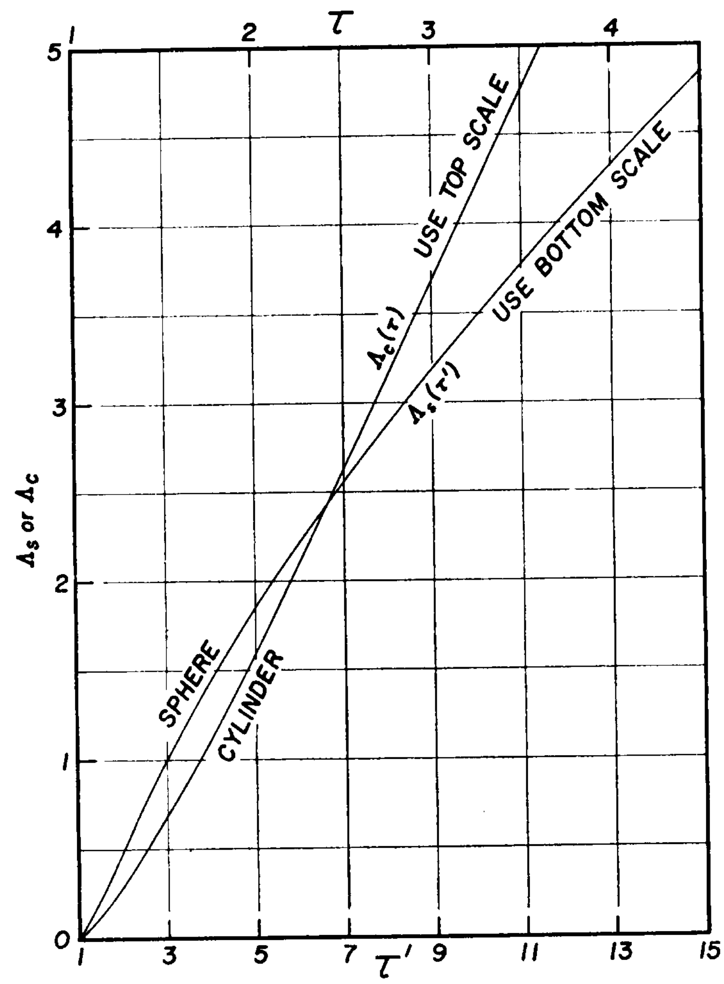

FIG. 24

where F is the solution of the equation

$$T^2F^{1/2}\,\mathrm{d}^2F/\mathrm{d}T^2 = 1 \tag{18}$$

subject to the boundary conditions $F = F' = 0$ at $T = 1$. The function $\Lambda_c(\tau)$ is defined as

$$\Lambda_c(\tau) = \tau^{2/3}G(\tau), \tag{19}$$

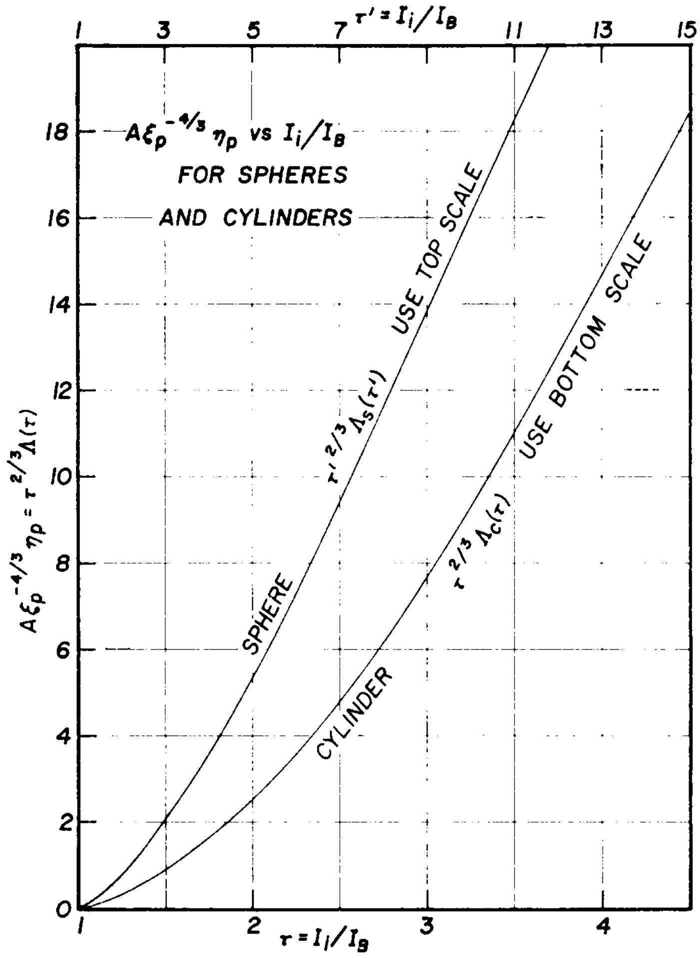

FIG. 25

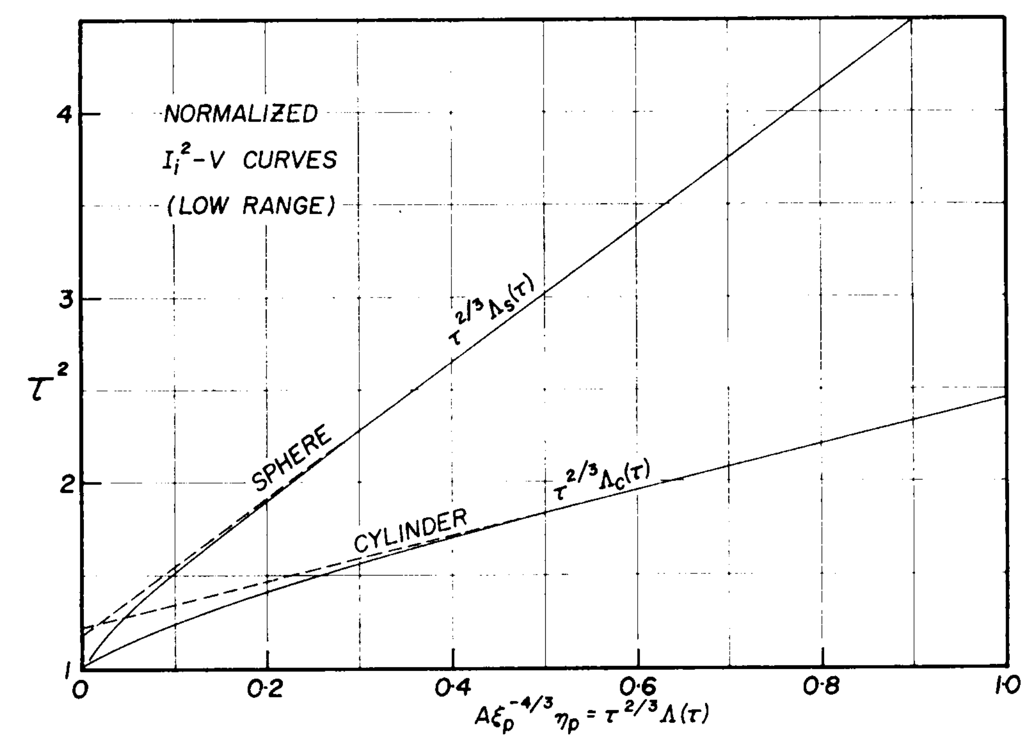

FIG. 26

where G is the solution of the equation

$$\psi^2 G^{1/2} \frac{\mathrm{d}}{\mathrm{d}\psi}\left(\psi \frac{\mathrm{d}G}{\mathrm{d}\psi}\right) = 1 \tag{20}$$

under the same boundary conditions. The curves in the LAM diagram (Fig. 19) are of the functions $\tau^{2/3}\Lambda_s(\tau)$ and $\tau^{2/3}G(\tau)$. The dashed portions of the curves in Figs. 19, 22 and 23 indicate the region where trapped ions are possible.

Since very often ion trapping does not occur even when it can, it is possible to use much higher voltages or smaller probes than the trapping criterion dictates. The functions $\Lambda_s(\tau)$ and $\Lambda_c(\tau)$ for this extended range of τ, where trapping can occur, are shown in Fig. 24. The curves $\tau^{2/3}\Lambda_s(\tau)$ and $\tau^{2/3}\Lambda_c(\tau)$, which are the ones in the first quadrant of the LAM diagram (Fig. 19) are shown for this extended range in Fig. 25.

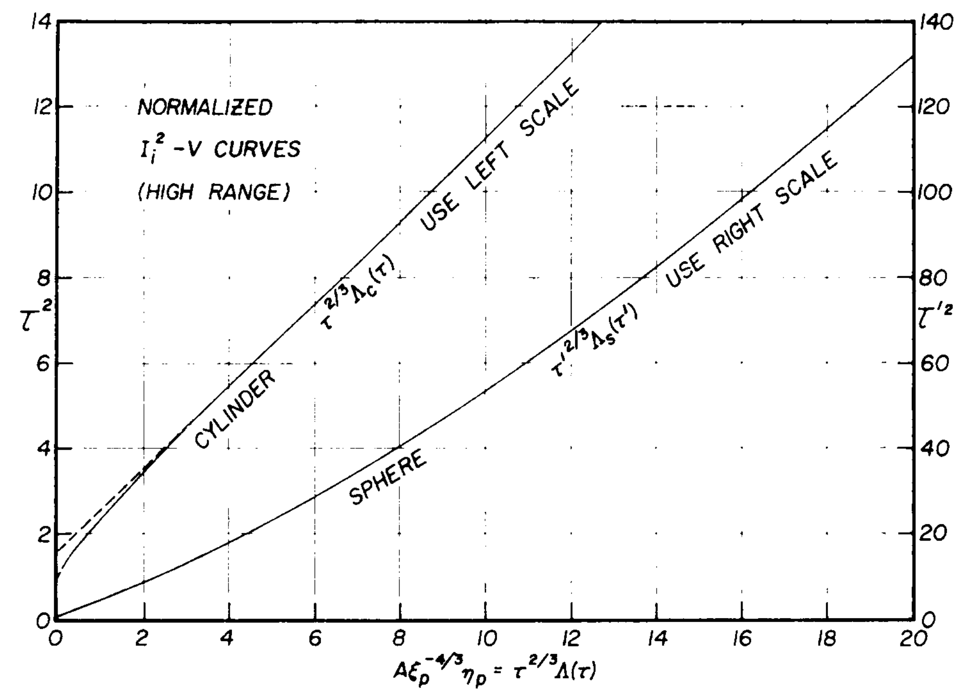

FIG. 27

In Fig. 26 we show τ^2 vs. $A\xi_p^{-4/3}\eta_p$ in the 'normal' range of τ. This is essentially an I_i^2-V_p plot and shows that such a plot can be approximated by a straight line. In Fig. 27 we show the same plot for the extended range of τ.

All of the results in this paper are subject to the restriction $\eta_p \gtrsim 4$ so that the electron distribution is approximately Maxwellian.

Larger reproductions of these graphs may be found elsewhere (CHEN, 1964).

Acknowledgments—The author is indebted to Mrs. J. PESKIN for performing the calculations for finite β on an IBM 704 computer, to Mr. H. FISHMAN for the calculation for $\beta = 0$ on an IBM 7090, and to Mr. K. P. MANN for plotting and tracing the numerous curves. This work was supported by the U.S. Atomic Energy Commission.

REFERENCES

ALLEN J. E., BOYD R. L. F. and REYNOLDS P. (1957) *Proc. phys. Soc. Lond.* **70B,** 297.
BERNSTEIN I. B. and RABINOWITZ I. (1959) *Phys. Fluids* **2,** 112.
BOHM D. BURHOP E. H. S. and MASSEY H. P. W. (1949) in *The Characteristics of Electrical Discharges in Magnetic Fields* (A. Guthrie and R. K. Wakerling, Eds.), Chap. 2, McGraw-Hill, New York.
BOYD R. L. F. and THOMPSON J. B. (1959) *Proc. roy. Soc.* **252A,** 102.
CHEN F. F. (1964) Princeton University Plasma Physics Laboratory Report MATT-252.
HALL L. S. (1964) University of California Radiation Laboratory Report UCRL-7660-T.
ICHIMIYA T., TAKAYAMA K. and AONO Y. (1960) in *Space Research: Proceedings of the First International Space Science Symposium*, Nice 1960, p. 397, North Holland, Amsterdam.
KAGAN YU. M. and PEREL V. I. (1953) *Dokl. Akad. Nauk SSSR* **91,** 1321.
LAM S. H. (1964) Princeton University Gas Dynamics Laboratory Report No. 681. To be published.
LANGMUIR I. (1961) *Collected Works* (G. SUITS, Ed.), Vol. 4, p. 99, Pergamon Press, Oxford.
SCHULZ G. J. and BROWN S. C. (1955) *Phys. Rev.* **98,** 1642.
WENZL F. (1950) *Z. angew. Phys.* **2,** 59.